Electronic Supplementary Information

Solar-Responsive Treble Photocatalytic Action of Sulfur-Bridged-2DRB Framework Composites for Selective 1,4 NADH Regeneration with Simultaneous Benzyl alcohol Production and Boronic Acid Conversion

Rehana Shahin,[a] Rajesh K. Yadav[a*], Shaifali Mishra[a], Kanchan Sharma[a], Chandani Singh[b], Vinay K. Mishra[a], Surendra K. Jaiswal[a], Geeta Srivastaw[a], Anupma Yadav[a], Jin-OoK Baeg[b*]

[1*]Department of Chemistry and Environmental Science, Madan Mohan Malaviya University of Technology, Gorakhpur 273010, India. *Email: rajeshkr_yadav2003@yahoo.co.in

[2*]Korea Research Institute of Chemical Technology, N3, 141 Gajeong-ro, Yuseong-gu, Daejeon 34114, Korea South Korea. *Email: jobaeg@krict.re.kr

1.Instruments and measurements

UV-Visible spectra were recorded on Shimadzu UV-1800 spectrometer. Fourier transform infrared spectroscopy (FTIR) spectra were obtained on a Shimadzu IR Spirit. Powder X-ray diffractometer (Bruker, AXS D8 Advance X-ray diffractometer and Cu Kα radiation) was used for crystallinity. Scanning electron microscope (SEM) images and electron dispersive X-ray spectroscopy (EDS), along with elemental mapping, were recorded using an instrument JSM 6490 LV (constructed by JEOL, Japan). The thermogravimetric analysis (TGA) was carried out on TA Instruments Q500 instrument over a range of 25-800 ºC with a heating rate of 5ºC min^{-1}. Diffraction electron spectroscopy (DSC) analysis was recorded on (Shimadzu Japan model DSC-60 Plus) instrument over a heating rate of 25-800 ºC of 5ºC min^{-1}. Ramam spectra were recorded in SENTERA (Bruker). Cyclic Voltammetry, Tafel plots, Electrochemical Impedance Spectroscopy (EIS), and chronopotentiometry were performed on (CHI608E-220V) instrument. Proton nuclear magnetic resonance (^{1}H NMR) spectra were recorded on a Bruker AVANCE II + 500 MHz spectrometer. X-ray photoelectron spectroscopy (XPS) was performed using an Escalab 250Xi instrument from Thermo Fisher. HPLC recorded on 7890A, Agilent Technologies. Photoluminescence spectrum (PL) was recorded on Perkin Elmer LS-55. BET analysis recorded on Quantachrome Instruments v5.25.

2. Material

Rose Bengal (RB), Sulphur powder (S), Benzaldehyde, Ascorbic acid (AsA), Rhodium complex, alcohol dehydrogenase (ADH), triethylamine (TEA), chloroform, nicotinamide adenine dinucleotide (NAD$^+$), Sodium phosphate buffer (SPB), boronic acid, Dimethylformamide (DMF) were purchased from Sigma-Aldrich, and TCI, which is used without further purification.

3. Solid UV - Visible spectra and determination of Tauc plot

Tauc plot show photon energy on x-axis and quantity (ahv)$^{1/2}$ on y-axis. Where, α represented the absorption coefficient. By exploration the y-axis quality, the optical band gap was calculated. Tauc-derived values are employed solely for comparative assessment of band-gap tuning and visible-light absorption enhancement relevant to photocatalytic performance. (1–6)

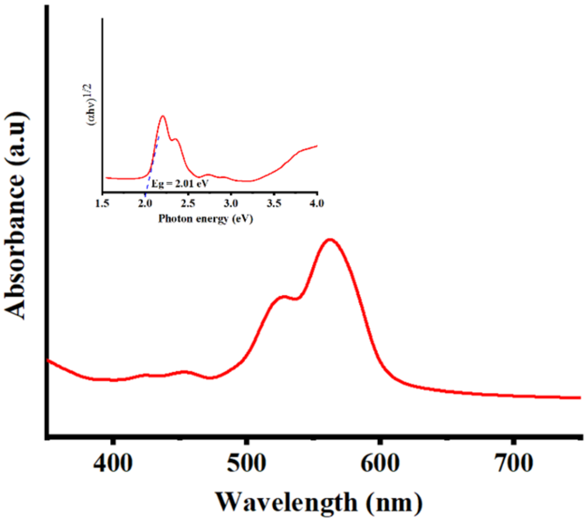

Fig. S1 DRS spectra of RB with insect Tauc plot.

4. UV-Visible spectrum and ^{1}H-NMR of regenerated 1,4-NADH

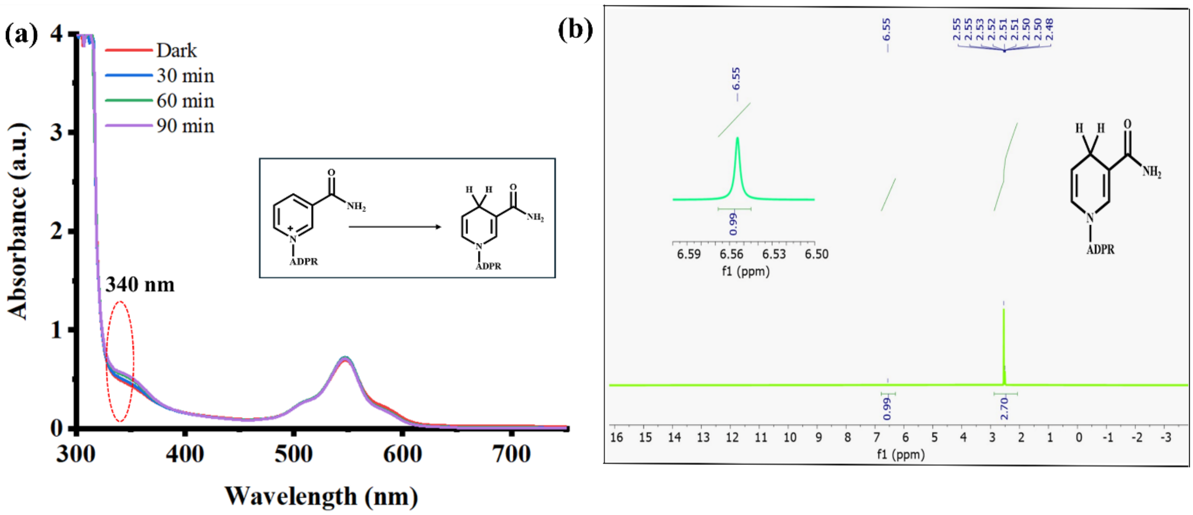

Fig. S2 (a) UV-visible spectra for NADH detection, and (b) ^{1}H-NMR of regenerated 1,4-NADH.

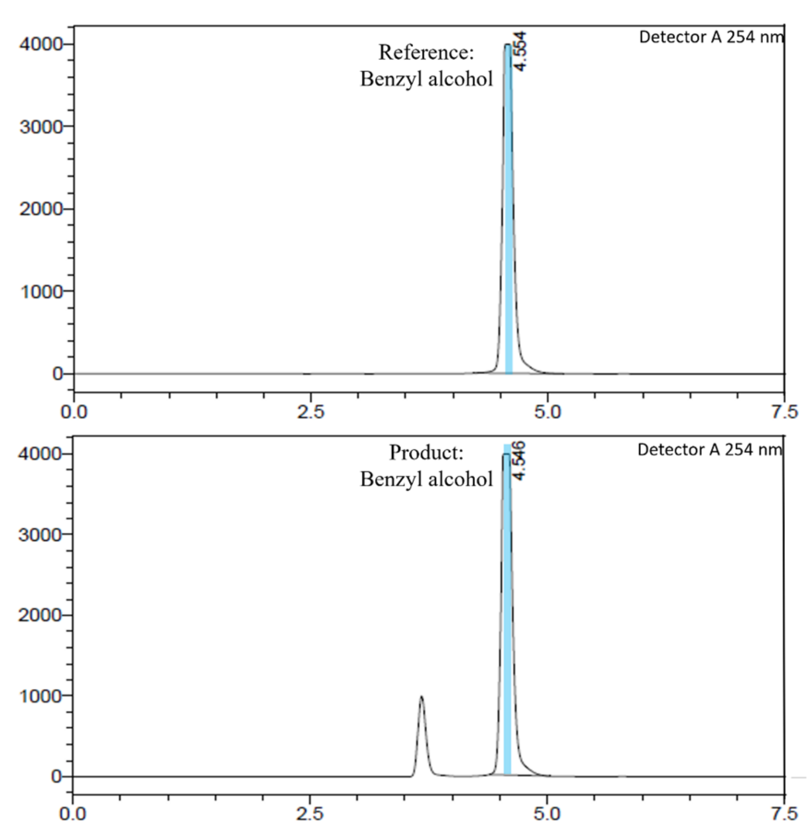

Fig. S3 HPLC Chromatogram of standard benzyl alcohol (reference), and photo catalytically synthesized benzyl alcohol equipped with C18 column with mobile phase acetonitrile: water (55:45 v/v).

5. Raman analysis

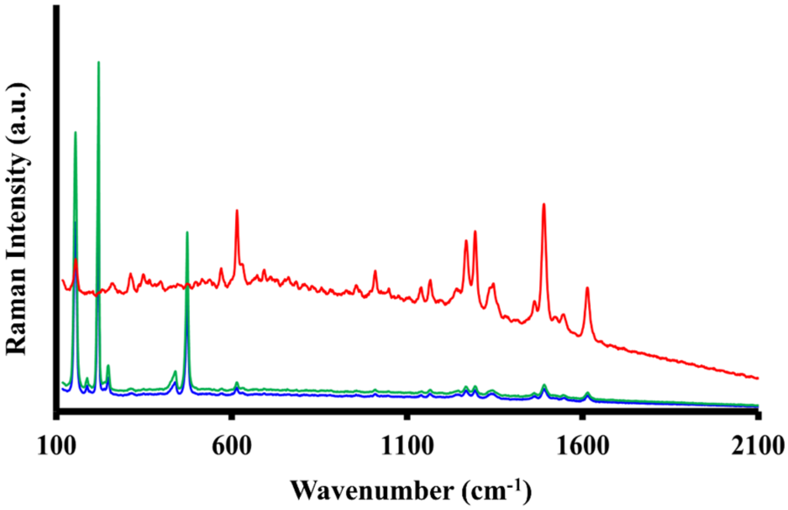

Fig. S4 Raman spectrum of S, RB and SB-2DRB photocatalyst.

6.SEM-EDX and elemental mapping

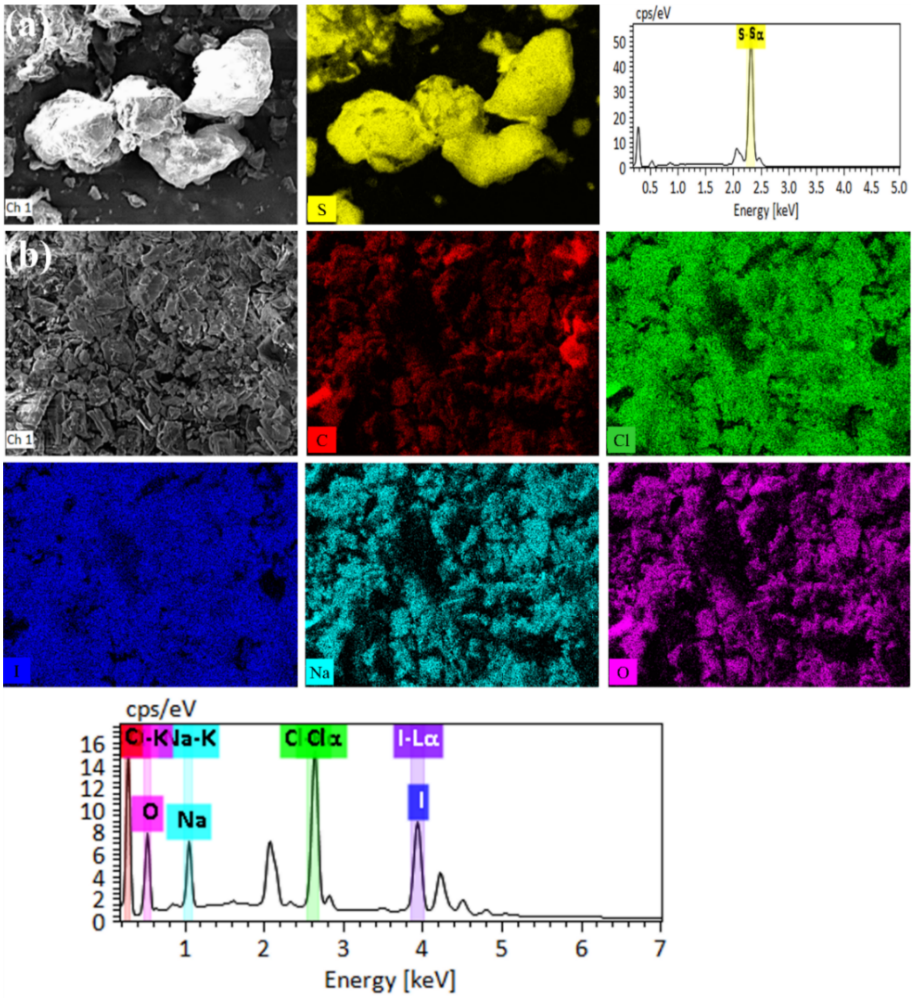

Fig. S5 Elemental mapping by SEM-EDX of (a) S and (b) RB.

7. TEM microscopic analysis

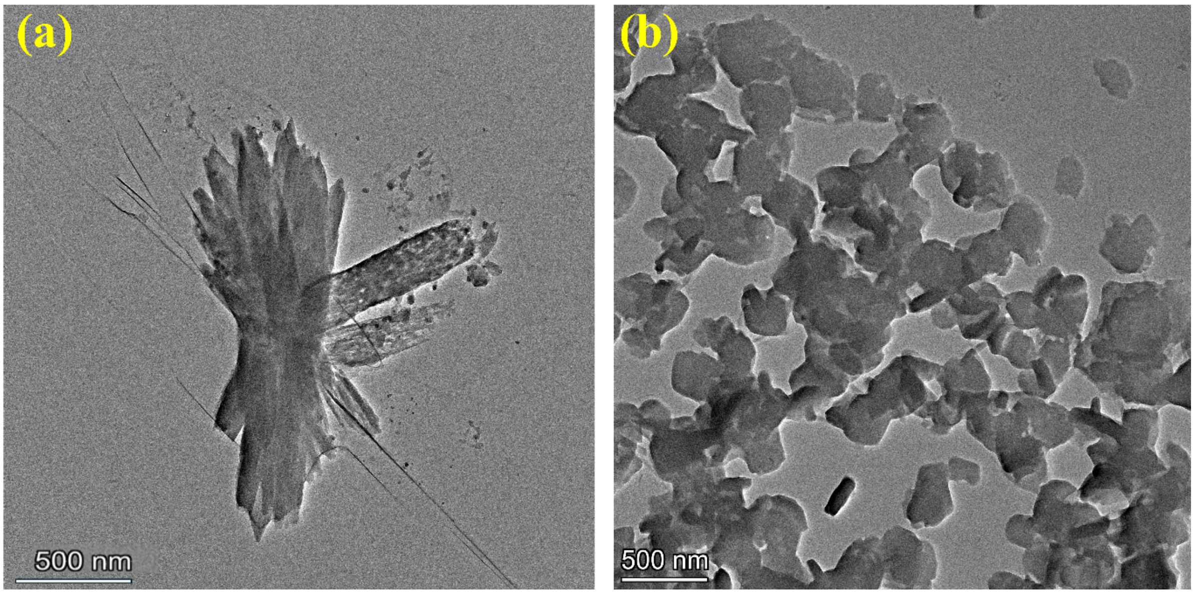

Fig. S6 TEM image of (a) S, and (b) RB.

8. Cyclic voltammetry analysis

Based on experiment of cyclic voltammetry the redox potential (oxidation and reduction potential) and charge transfer characteristic of solar light harvesting SB-2DRB photocatalyst examined by using a Hg/Hg_2Cl_2 reference electrode, dipped in 0.1M tetrabutylammonium hexafluorophosphate electrolyte at a voltage range of −2.0 to +2.0 V with 0.1 mV/s scanning rate. From the cyclic voltagram of SB-2DRB composite photocatalyst, the one onset oxidation potential was clearly observed approximately at - 1.06 eV and one onset reduction potential observed approximately at + 1.36 eV (Fig. 9a, blue line). The E_{HOMO} and E_{LUMO} calculated by formula as follows:

$$E_{HOMO} = - [E_{ox} + 4.5]\ eV = - [1.52+4.5] = -6.02\ eV$$

$$E_{LUMO} = - [E_{red} + 4.5]\ eV = - [1.10+4.5] = -3.40\ eV$$

$$\text{Energy band gap} = [\ E_{HOMO} - E_{LUMO}]$$

$$= - [6.02- (-3.40)]$$

$$= 2.62\ eV$$

9. Electrochemical Impedance Spectroscopy (EIS)

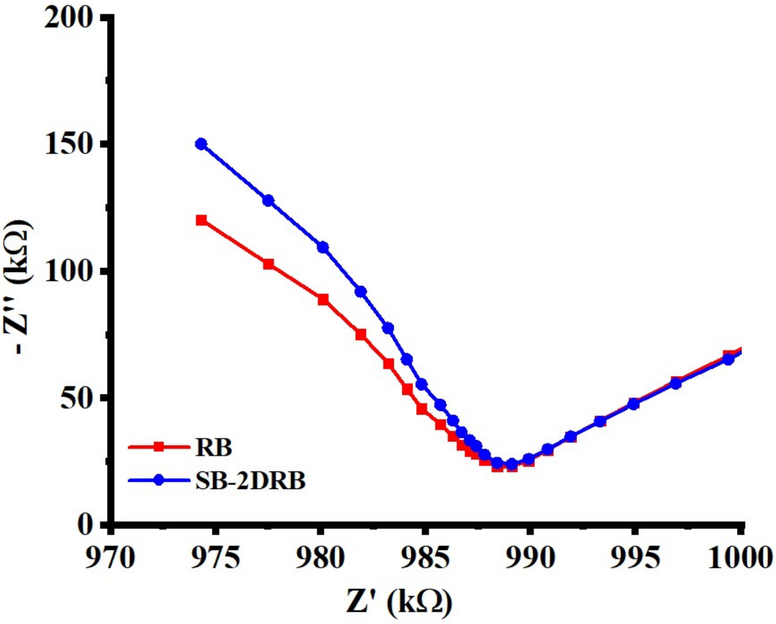

Fig. S7 Nyquist plot of RB (red line) and SB-2DRB composite photocatalyst (blue line).

Fig. S8 Nyquist (Z’ vs. Z’’), Bode phase (theta vs. frequency), and Bode magnitude (|Z| vs. frequency) graphs for RB and SB-2DRB photocatalyst. The Nyquist plots show short low-frequency tails after depressed semicircles, which are suggestive of charge-transfer-controlled processes with suboptimal interfacial capacitive behavior. The equivalent circuit Rs – (Roct || CPE), where Rs is the ohmic resistance, Roct is the charge-transfer resistance at the catalyst–electrolyte interface, and the CPE takes surface heterogeneity and non-ideal capacitance into account, was used to fit all spectra using ZView software. According to the fitted parameters, (Table S1) the RB sample displays Rs = 1152 Ω and Rct = 20.49 kΩ, whereas the SB-2DRB (PC) sample displays Rs = 986.3 Ω and Rct = 20.26 kΩ. CPE exponents (P ≈ 0.87) indicate fairly diverse interfaces. In line with its improved photocatalytic efficacy, SB-2DRB's somewhat lower Rs and similar Rct support more effective electron transport and decreased interface resistance. Further supporting the validity of the electrochemical interpretation and the dependability of the equivalent-circuit fitting is the outstanding agreement between the experimental and fitted curves in both Nyquist and Bode plots.

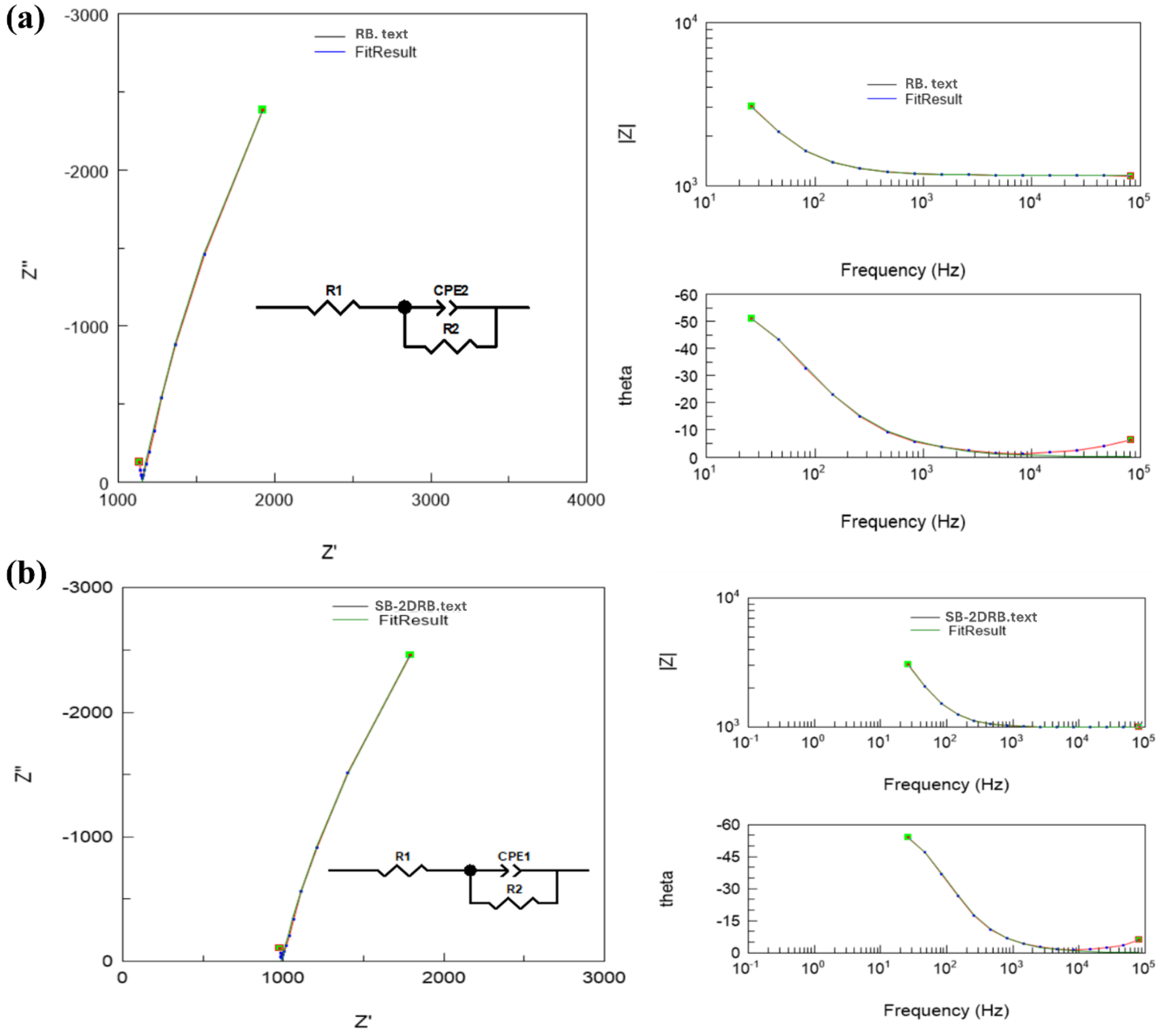

Fig. S8 Nyquist plots (left), Bode magnitude and phase plots (right) of EIS spectra for (a) RB, (b) SB-2DRB photocatalysts are shown. Experimental data are shown as scatter points and fitted curves obtained using ZView software. Equivalent circuit models used for fitting are shown as insets, incorporating solution resistance (Rs), charge-transfer resistance (Roct), and constant phase element (CPE), capturing both interfacial and diffusion-related processes.

Table S1. Values of elements in equivalent circuit resulted from fitting the EIS data.

	RB	2D-SBRB
R1 (Rs)	1152 Ω	986.3 Ω
R2(Rct)	20.49 kΩ	20.26 kΩ
CPE1-T	4.2895E- 10^{-6}	4.4768E-10^{-6}
CPE1-P	0.878	0.877

10. Substrate scope of product

Table S2. Substrate scope for aryl boronic acid conversion into phenol.

entry	Boronic acid derivative	Phenol Product	%Yield
a.	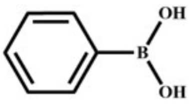	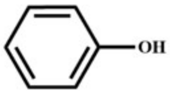	**96**
b.	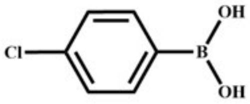		**94**
c.	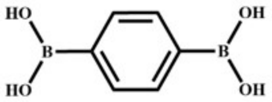		**91**
d.	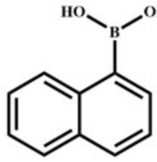	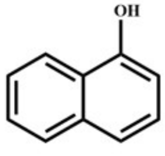	**84**

Reaction conditions: Phenylboronic acid derivatives (0.1 mmol), SB-2DRB (2 mg), TEA (0.21 mL), visible light, room temperature. isolated yields were given.

11. ^{1}H-NMR characterization data of the product

a. Phenol: (Yield 96%),,^{1}H NMR (500 MHz, $CDCl_3$) δ 8.12-8.13 (m, 2H), 7.47-7.62 (m,2H), 7.50 (s, 1H), 5.41 (s, 1H).

b. Chlorophenol: (Yield 94%), ^{1}H NMR (500 MHz, DMSO) δ 7.13-7.19 (d,2H), 6.65-6.77 (d, 2H), 5.31 (s, 1H)

c. Hydroquinone: (Yield 91%), ^{1}H NMR (500 MHz, DMSO-d^6) δ 8.31 (s, 2H), 8.06 (s, 2H), 5.30 (s, 2H).

d. 1-Naphthol: (Yield 84%), ^{1}H NMR (500 MHz, $CDCl_3$-d,) δ: 7.61-7.63 (m, 1H), 7.67-7.69 (m, 6H), 9.91 (s, 1H).

12. NMR spectra of synthesized phenol derivatives

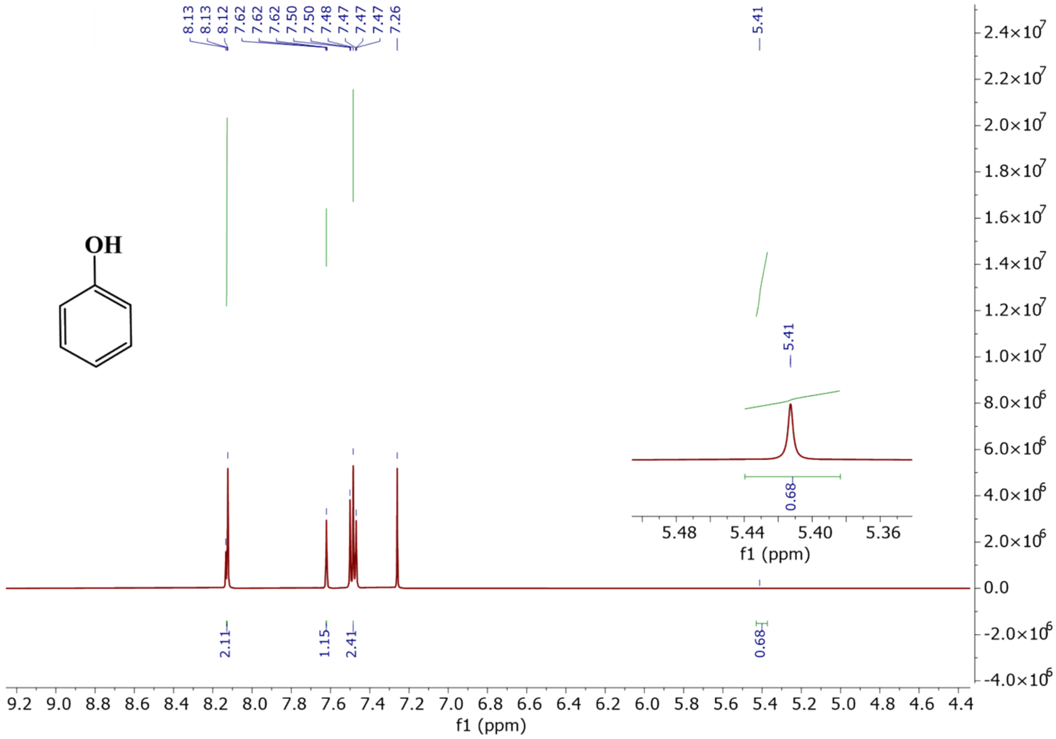

Fig. S9 ^{1}H NMR spectrum of phenol.

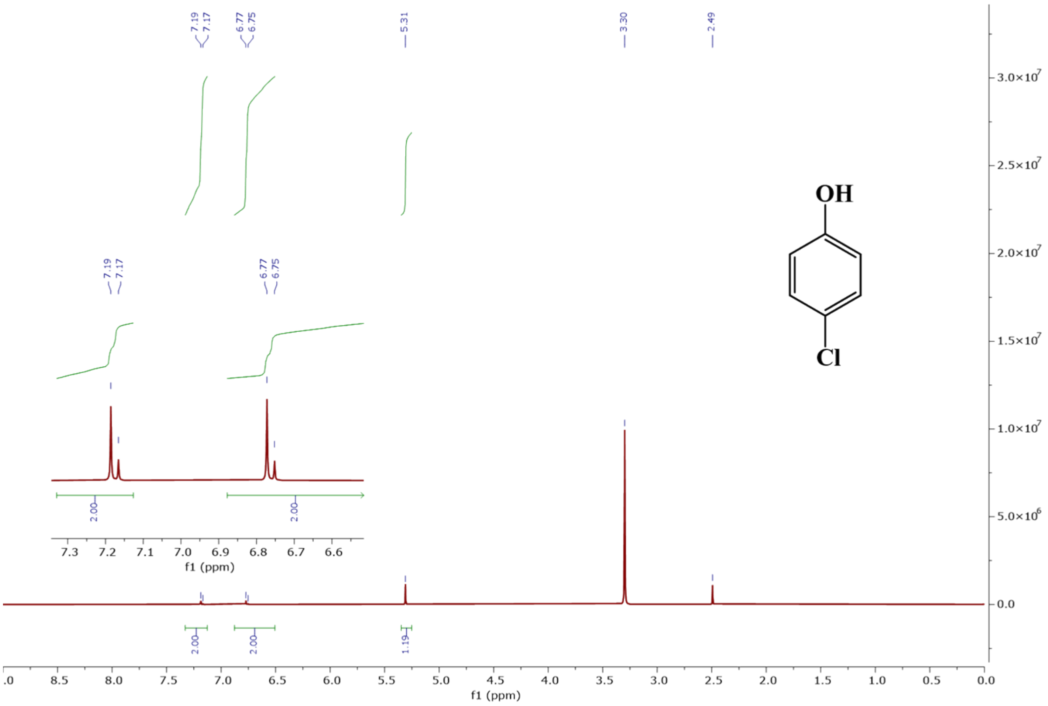

Fig. S10 ^{1}H NMR spectrum of 4-chlorophenol.

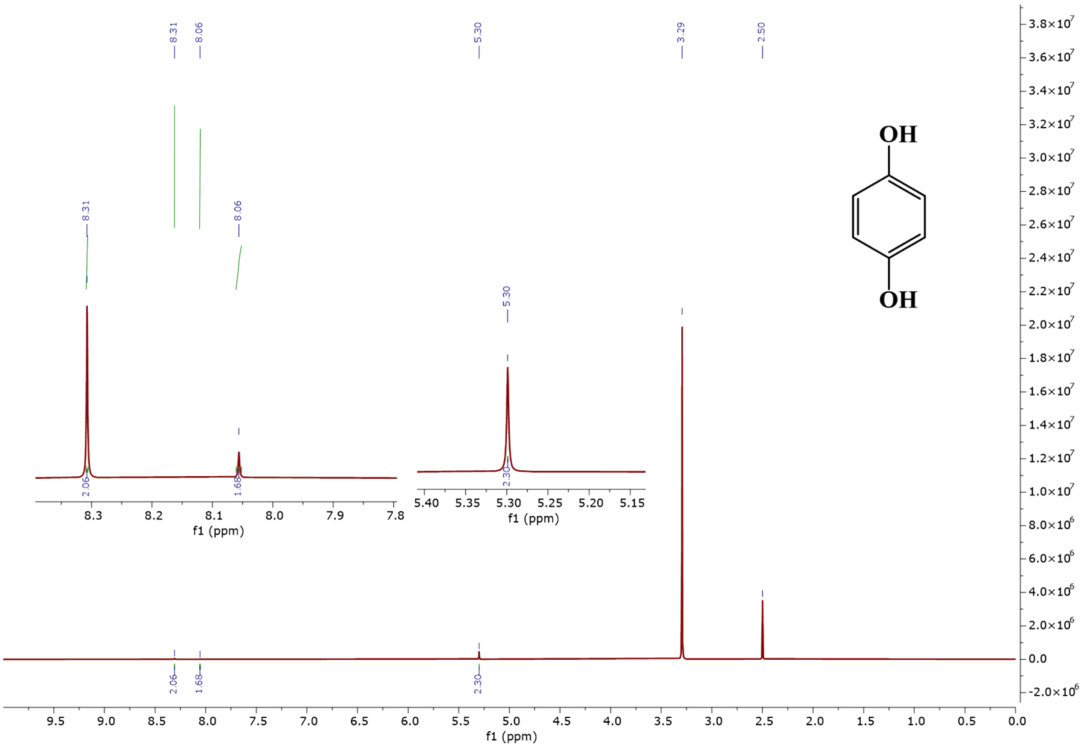

Fig. S11 ^{1}H NMR spectrum of hydroquinone.

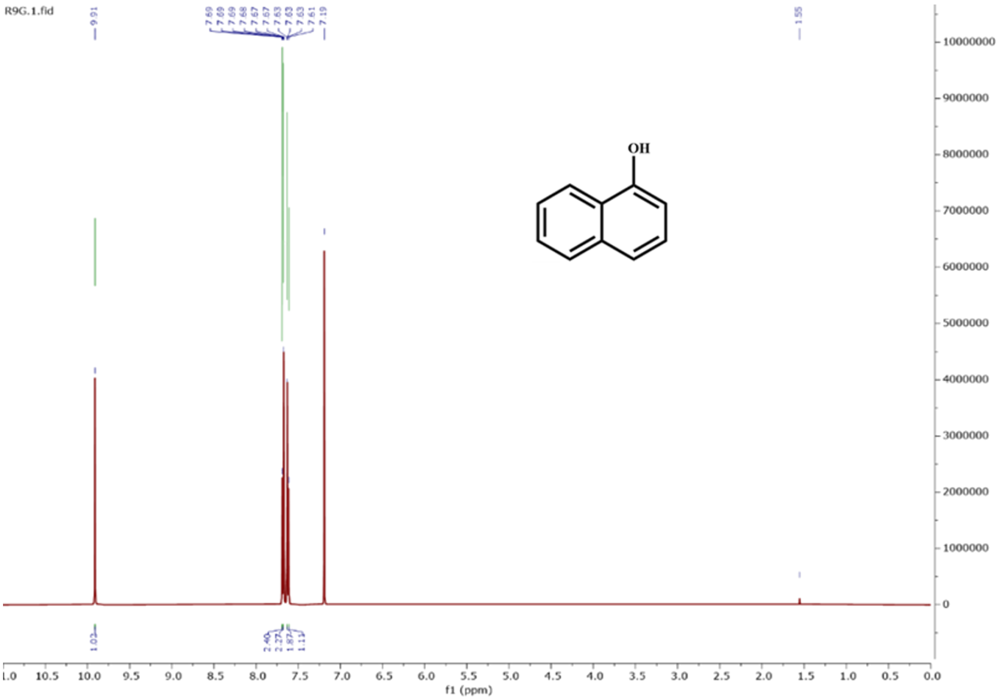

Fig. S12 ^{1}H NMR spectrum of 1-Naphthol.

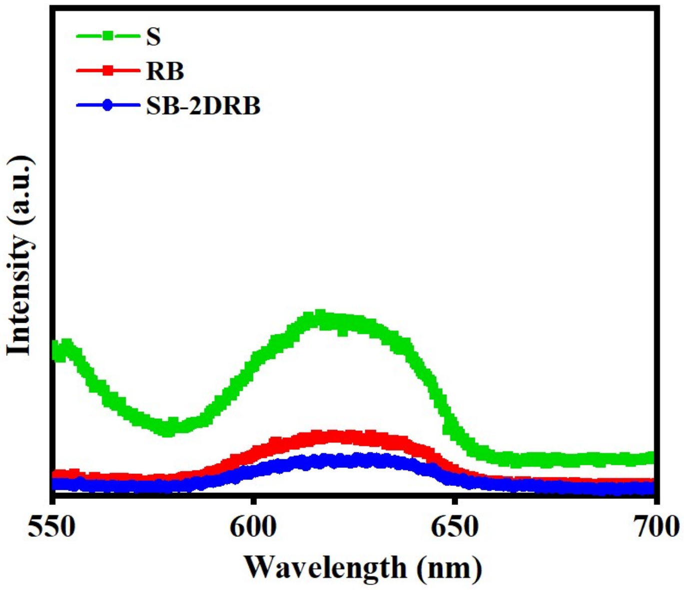

Fig. S13 Photoluminescence spectra of S, RB, and SB-2DRB.

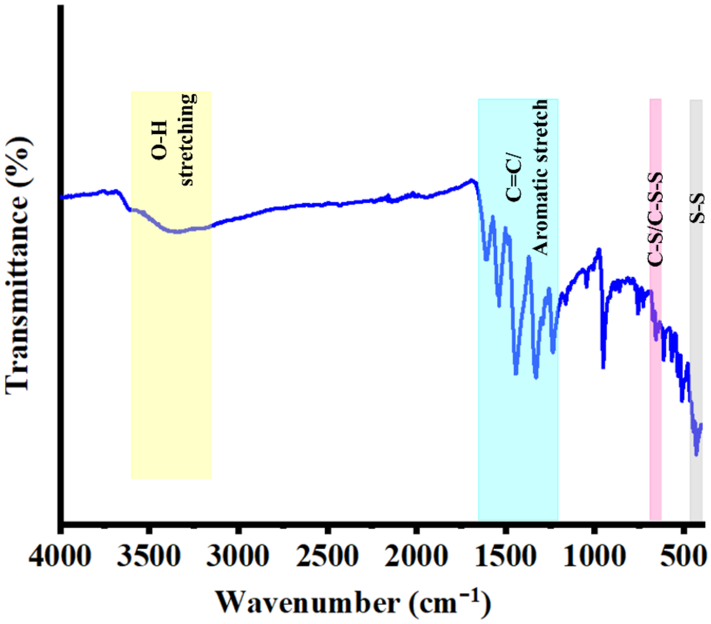

Fig. S14 FTIR spectra of SB-2DRB.

Table S3. BET Surface Area, Pore Volume, and Pore Size of RB and SB-2DRB.

Material	S_{BET} (m^2g^{-1})	Pore volume (cm^3g^{-1})	Pore size (nm)
RB	1.475	0.003	9.8
SB-2DRB	3.311	0.013	16.7

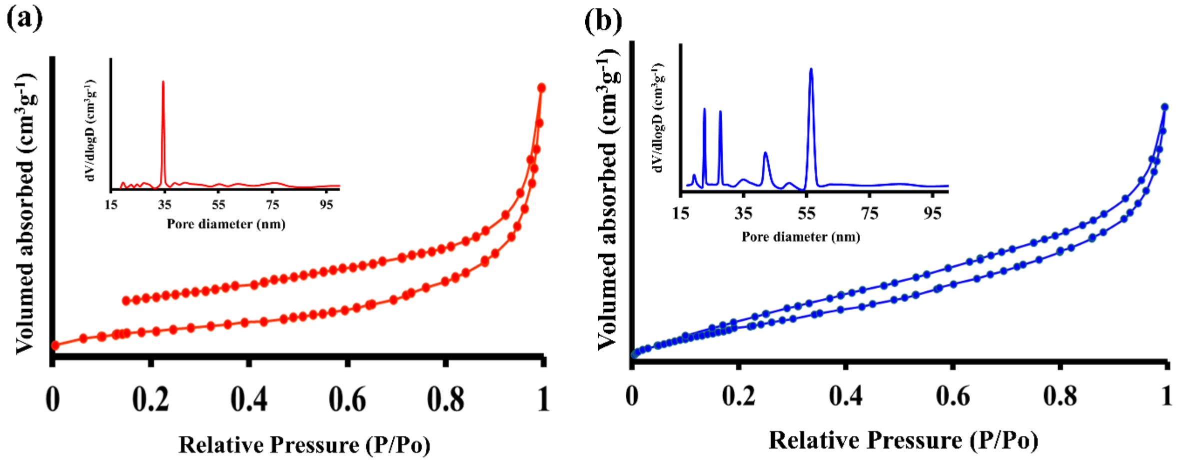

Fig. S14 Nitrogen adsorption desorption isotherms of (a) RB, and (b) SB-2DRB photocatalyst measured at 77 K with corresponding pore size distribution inset.

13. Reusability and cyclic stability test

The reusability of the SB-2DRB composite photocatalyst for NADH regeneration was evaluated by recovering the photocatalyst after each catalytic cycle through centrifugation method followed by washing. The recovered photocatalyst was then dried in an oven and reused for subsequent cycles. This procedure was repeated for five consecutive cycles to assess the stability and photocatalytic performance of the recycled catalyst. The results indicated that the yield remained stable, demonstrating good reusability. Both the before catalysis and after catalysis, XRD patterns exhibit characteristic diffraction peaks typical of SB-2DRB, indicating that its crystalline structure remains largely intact after repeated photocatalytic cycles. The absence of any significant shift in peak positions confirms that no major phase transformation occurred during the NADPH regeneration process. Although a slight decrease in the intensity of the main diffraction peak is observed after catalysis, this may be attributed to minor surface disorder or a small loss of crystallinity. Overall, the XRD results validate the structural stability of SB-2DRB and confirm its suitability for repeated use in photocatalytic applications.

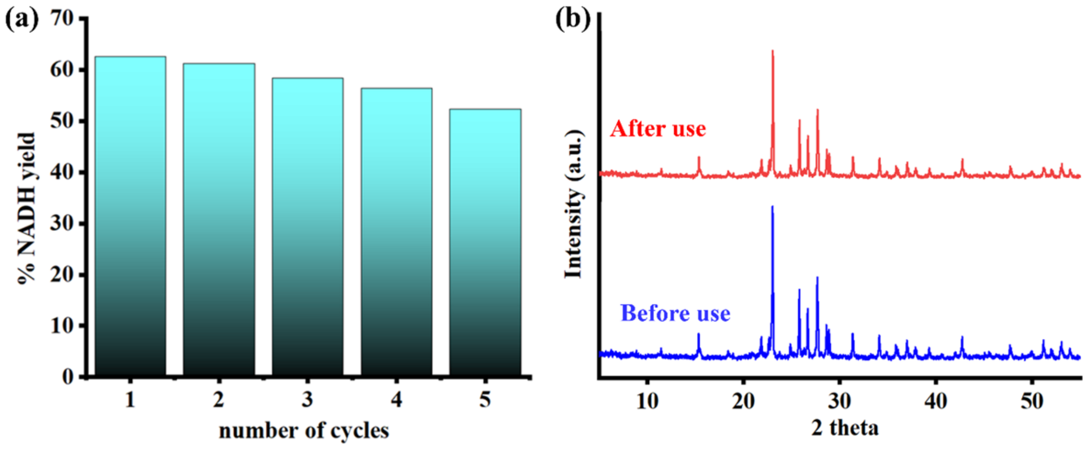

Fig. S15 (a) Recyclability for NADH regeneration up to five cycles and (b) photochemical stability through XRD of RB-2DSB photocatalyst before and after photocatalytic experiment.

14. Importance of Sulfur-Bridged-2DRB Photocatalyst Recovery and Applicable

The recovery of catalyst is a key factor for industrial implementation, as it affects process cost, sustainability, and operational feasibility. As a heterogeneous system, the SB-2DRB composite photocatalyst can be readily recovered using conventional techniques such as filtration or centrifugation. Its stable sulfur-bridged (-S-S-) framework ensures structural integrity and consistent performance over multiple cycles. [18,19] During the reusability studies, the SB-2DRB photocatalyst was recovered by a simple centrifugation method, followed by washing and drying, and then reused in subsequent photocatalytic cycles without significant loss of activity.

15. Control experiments

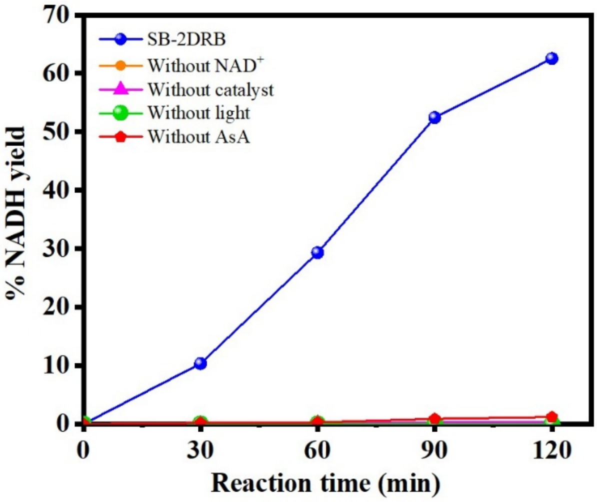

Fig. S17 Control experiment for NADH regeneration yield based on different reaction conditions. (Reaction condition: 31 µL of the SB-2DRB, 310 µL of ascorbic acid, 248 µL of NAD$^+$, 124 µL of rhodium complex in 3.1 mL of different pH of buffer solution).

The optimal photocatalyst dose for NADH formation was 2.0 mg of SB-DRB. Beyond this optimal dose, photocatalyst agglomeration hinders reactant access to the catalyst surface and suppresses electron–hole pair regeneration, which ultimately reduces the yield.

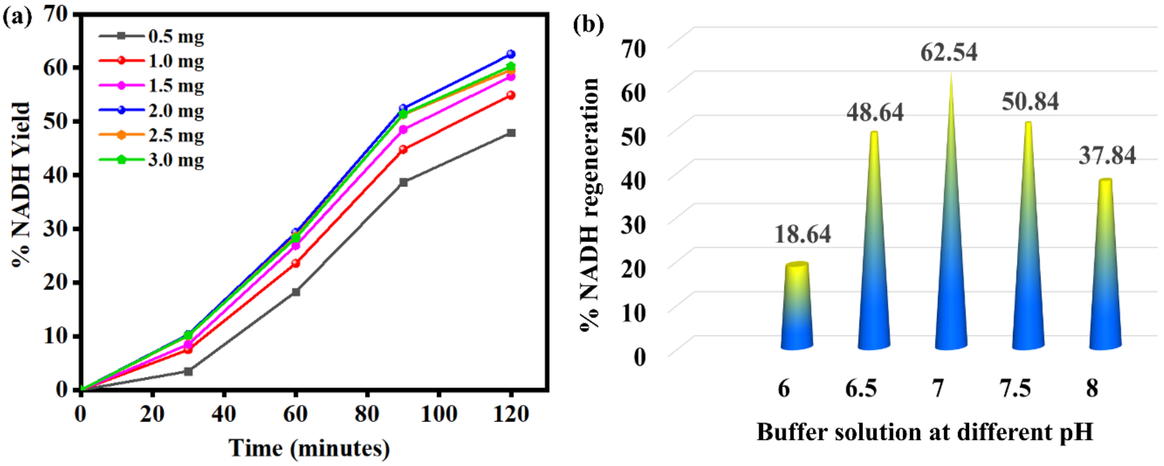

Fig. S16 % NADH regeneration yield under different reaction conditions (a) With different SB-2DRB dosage, and (b) buffer solution with different pH values. (Reaction condition: 31 µL of the SB-2DRB, 310 µL of ascorbic acid, 248 µL of NAD$^+$, 124 µL of rhodium complex in 3.1 mL of buffer solution).

Table S4. Comparison of band gap energy to Evaluate photocatalytic performance.

S. No	Photocatalyst	Energy band gap	Ref.
1.	Elemental Sulfur (S)	2.7-2.8 eV	(7, 8)
2.	Rose Bengal (RB)	2.01 eV	(9–11)
3.	**SB-2DRB**	2.5eV	This work

Table S5. Comparative analysis various reported photocatalyst for photocatalytic performance.

Entry	Photocatalyst	Time (h)	NADH	Benzyl alcohol production	Phenol synthesis	Ref.
1.	CN	1	7.91	---	---	(12)
3.	Fmoc-FF/g-C_3N_4	3	62.7	---	---	(13)
4.	CCG-MP	2	45.54	---	---	(14)
6.	CdS nanocrystals	2	53	---	---	(15)
7.	SnC	78	73	---	---	(16)
8.	TCPP/SiO_2/Rhg	75	75	---	---	(17)
9.	N-GDY	2	30	---	---	(18)
10.	PDI/CN	9	75	---	---	(19)
11.	CN-TiO_2-MS	2	40.0	---	---	(20)
12.	Pt/ana-350	6	56.7	---	---	(21)
13.	p-doped TiO_2	9	34.6	---	---	(22)
14.	**SB-2DRB**	2	62.54	166.7 mL	96 (6h)	This work

Table S6. Comparative analysis various reported photocatalyst for boronic acid conversion.

Entry	Photocatalyst	Time (h)	% Yield	Ref.
1.	CPOP-28	48	76	[9]
2.	BBO-COF	96	99	[10]
3.	gC_3N_4LMPET	12	42	[11]
4.	3D-COF	72	40	[12]
5.	Cz-POF-1	24	28	[13]
6.	Tx-COF-2	72	74	[14]
7.	LZU-190	72	88	[15]
9.	**SB-2DRB**	10	96	This work

References

1. Kumar A, Yadav R K, Park N-J and Baeg J-O 2017 Facile one-pot two-step synthesis of novel in situ selenium-doped carbon nitride nanosheet photocatalysts for highly enhanced solar fuel production from CO2 ACS Appl. Nano Mater. 1 47–54

1. Mamand, D. M., Muhammad, D. S., Muheddin, D. Q., Abdalkarim, K. A., Tahir, D. A., Muhammad, H. A., Aziz, S. B., Hussen, S. A. and Hassan, J. (2025) Optical band gap modulation in functionalized chitosan biopolymer hybrids using absorption and derivative spectrum fitting methods: A spectroscopic analysis. *Sci. Rep.* **15**, 3162. https://doi.org/10.1038/s41598-025-87353-5.

2. Klein, J., Kampermann, L., Mockenhaupt, B., Behrens, M., Strunk, J. and Bacher, G. (2023) Limitations of the Tauc Plot Method. *Adv. Funct. Mater.* **33**, 2304523. https://doi.org/https://doi.org/10.1002/adfm.202304523.

3. Makuła, P., Pacia, M. and Macyk, W. (2018) How To Correctly Determine the Band Gap Energy of Modified Semiconductor Photocatalysts Based on UV-Vis Spectra. *J. Phys. Chem. Lett.* **9**, 6814–6817. https://doi.org/10.1021/acs.jpclett.8b02892.

4. Samia, Usman, M., Osman, A. I., Khan, K. I., Saeed, F., Zeng, Y., Motola, M. and Dai, H. (2024) Enhanced visible-light photocatalytic degradation of organic pollutants using fibrous silica titania and Ti3AlC2 catalysts for sustainable wastewater treatment. *New J. Chem.* **48**, 17500–17515. https://doi.org/10.1039/D4NJ03277B.

5. Ding, J., Guan, X., Lv, J., Chen, X., Zhang, Y., Li, H., Zhang, D., Qiu, S., Jiang, H.-L. and Fang, Q. (2023) Three-Dimensional Covalent Organic Frameworks with Ultra-Large Pores for Highly Efficient Photocatalysis. *J. Am. Chem. Soc.* **145**, 3248–3254. https://doi.org/10.1021/jacs.2c13817.

6. Lin, W., Lin, F., Lin, J., Xiao, Z., Yuan, D. and Wang, Y. (2024) Efficient Photocatalytic CO2 Reduction in Ellagic Acid–Based Covalent Organic Frameworks. *J. Am. Chem. Soc.* **146**, 16229–16236. https://doi.org/10.1021/jacs.4c04185.

7. Guo, J., Lu, Z., Li, C., Miao, Y., Zhang, B., Lam, J. W. Y., Shi, Y. E., Wang, Z. and Tang, B. Z. (2022) Long-Lived Afterglow from Elemental Sulfur Powder: Synergistic Effects of Impurity and Structure. *ACS Omega*. https://doi.org/10.1021/acsomega.2c04307.

8. Hu, C., Zheng, S., Lian, C., Chen, F., Lu, T., Hu, Q., Duo, S., Zhang, R. and Guan, C. (2015) α-S nanoparticles grown on MoS2 nanosheets: A novel sulfur-based photocatalyst with enhanced photocatalytic performance. *J.*

Mol. Catal. A Chem. **396**, 128–135. https://doi.org/https://doi.org/10.1016/j.molcata.2014.09.033.

9. Lu, C., Chen, R., Wu, X., Fan, M., Liu, Y., Le, Z., Jiang, S. and Song, S. (2016) Applied Surface Science Boron doped g-C 3 N 4 with enhanced photocatalytic UO 2 2 + reduction performance. **360**, 1016–1022. https://doi.org/10.1016/j.apsusc.2015.11.112.

10. Zou, J., Yu, Y., Yan, W., Meng, J. and Zhang, S. (2019) Chemical A facile route to synthesize boron-doped g-C 3 N 4 nanosheets with enhanced visible-light photocatalytic activity. *J. Mater. Sci.* **54**, 6867–6881. https://doi.org/10.1007/s10853-019-03384-0.

11. Quintana, M. A., Solís, R. R., Angeles, M., Bl, G., M, F. and Mu, M. J. (2022) Enhanced boron modified graphitic carbon nitride for the selective photocatalytic production of benzaldehyde. **298**. https://doi.org/10.1016/j.seppur.2022.121613.

12. Kumar, A., Yadav, R. K., Park, N. J. and Baeg, J. O. (2018) Facile One-Pot Two-Step Synthesis of Novel in Situ Selenium-Doped Carbon Nitride Nanosheet Photocatalysts for Highly Enhanced Solar Fuel Production from CO2. *ACS Appl. Nano Mater.* **1**, 47–54. https://doi.org/10.1021/acsanm.7b00024.

13. Ko, J. W., Choi, W. S., Kim, J., Kuk, S. K., Lee, S. H. and Park, C. B. (2017) Self-Assembled Peptide-Carbon Nitride Hydrogel as a Light-Responsive Scaffold Material. *Biomacromolecules* **18**, 3551–3556. https://doi.org/10.1021/acs.biomac.7b00889.

14. Yadav, R. K., Baeg, J.-O., Oh, G. H., Park, N.-J., Kong, K., Kim, J., Hwang, D. W. and Biswas, S. K. (2012) A photocatalyst--enzyme coupled artificial photosynthesis system for solar energy in production of formic acid from CO2. *J. Am. Chem. Soc.* **134**, 11455–11461.

15. Nam, D. H., Lee, S. H. and Park, C. B. (2010) CdTe , CdSe , and CdS Nanocrystals for Highly Efficient Regeneration of Nicotinamide Cofactor Under Visible. 922–926. https://doi.org/10.1002/smll.201000077.

16. Lee, M., Kim, J. U., Lee, J. S., Lee, B. Il, Shin, J. and Park, C. B. (2014) Mussel-Inspired Plasmonic Nanohybrids for Light Harvesting. 1–6. https://doi.org/10.1002/adma.201305766.

17. Ji, X., Wang, J., Mei, L., Tao, W., Barrett, A., Su, Z., Wang, S., Ma, G., Shi, J. and Zhang, S. (2018) Porphyrin/SiO2/Cp* Rh (bpy) Cl Hybrid nanoparticles mimicking chloroplast with enhanced electronic energy transfer for biocatalyzed artificial photosynthesis. *Adv. Funct. Mater.* **28**, 1705083.

18. Preparation of N-Graphdiyne Nanosheets at Liquid / liquid Interface for Photocatalytic NADH Regeneration

(2018). https://doi.org/10.1021/acsami.8b03311.

19. Zhang, P., Hu, J., Shen, Y., Yang, X., Qu, J., Du, F., Sun, W. and Li, C. M. (2021) Photoenzymatic catalytic cascade system of a pyromellitic diimide/g-C3N4 heterojunction to efficiently regenerate NADH for highly selective CO2 reduction toward formic acid. *ACS Appl. Mater. \& Interfaces* **13**, 46650–46658.

20. Nayak, J., Meher, S., Begum, G., Seth, S. and Rana, R. K. (2023) Bioinspired Mineralization and Assembly Route to Integrate TiO2 and Carbon Nitride Nanostructures: Designing Microstructures for Photoregeneration of NADH. *ACS Appl. Nano Mater.* **6**, 13708–13719.

21. Wang, M., Ren, X., Guo, M., Liu, J., Li, H. and Yang, Q. (2021) Chemoselective NADH Regeneration: the Synergy Effect of TiOx and Pt in NAD+ Hydrogenation. *ACS Sustain. Chem. Eng.* **9**, 6499–6506. https://doi.org/10.1021/acssuschemeng.1c02188.

22. Shi, Q., Yang, D., Jiang, Z. and Li, J. (2006) Visible-light photocatalytic regeneration of NADH using P-doped TiO2 nanoparticles. *J. Mol. Catal. B Enzym.* **43**, 44–48.